

Systematic Analysis of High Schmidt Number Turbulent Mass Transfer across Clean, Contaminated and Solid Interfaces

Yosuke Hasegawa and Nobuhide Kasagi

Department of Mechanical Engineering, The University of Tokyo

7-3-1 Hongo, Bunkyo-ku, Tokyo 113-8656, Japan

hasegawa@thtlab.t.u-tokyo.ac.jp, kasagi@thtlab.t.u-tokyo.ac.jp

Abstract - A series of numerical simulation is carried out for high Schmidt number turbulent mass transfer across interfaces of different dynamical conditions, i.e., a clean or contaminated free surface and also a solid surface. A distinct feature of free surface turbulence close to a contaminated interface is drastic damping of the surface divergence fluctuations at low frequencies, which play a critical role in the interfacial mass transfer. Various concentration statistics reveal that the transport mechanism at a highly contaminated interface becomes dynamically equivalent to that at a solid surface. Consequently, the interfacial mass transfer rate falls down to the value on a solid surface, so that the Schmidt number dependency of the mass transfer rate switches from $Sc^{-0.5}$ to $Sc^{-0.7}$. Based on a one-dimensional advection-diffusion equation, it is demonstrated that the ratio between typical intensity and frequency of the fluctuating surface divergence is a critical parameter for the transition of the turbulent mass transfer mode.

Keyword: turbulence; mass transfer; Schmidt number; air-water interface; surfactant

Notation

c	concentration of solute
C	mean concentration
C_B	bulk mean concentration
C_I	mean concentration at an interface
c_τ	friction concentration
D	molecular diffusivity
E_d	eddy diffusivity
k	kinetic energy
k_x, k_y, k_z	number of modes in streamwise, interface-normal and spanwise directions
L	integral length scale
p	pressure
q	local mass transfer rate (dimensionless local mass flux)
Q	global mass transfer rate (dimensionless global mass flux)
$R_{\alpha\beta}$	correlation coefficient between α and β
Re_T	Reynolds number based on macroscopic velocity scale u_T and integral length scale L
Re_τ	Reynolds number based on friction velocity u_τ and depth δ
n	Schmidt number exponent of mass transfer rate
N	number of grid points
Sc	Schmidt number
t	time
U	mean streamwise velocity
u, v, w	velocity components in the $x, y,$ and z directions
u_T	macroscopic velocity scale
u_τ	friction velocity
W_β	frequency spectrum of the surface divergence β
x, y, z	streamwise, interface-normal and spanwise directions
y_p	peak location of concentration fluctuation
<i>Greek</i>	
β	surface divergence

β_E	effective surface divergence
ΔC	difference between mean concentrations at an interface and a bottom boundary
ΔC_B	difference between interfacial and bulk mean concentrations
Δt	time step
$\Delta x, \Delta y, \Delta z$	grid spacings in streamwise, interface-normal and spanwise directions
δ	depth of computational domain
δ_c	thickness of diffusive sublayer
γ	surfactant concentration
ν	kinematic viscosity
ρ	fluid density
σ	surface tension
τ	interfacial shear stress
ω	frequency

Superscript

$()^*$	dimensional value
$()^+$	value non-dimensionalized by the shear unit
$()'$	fluctuating component
$\overline{()}$	mean component

Subscript

$()_a$	value in the air phase
$()_w$	value in the water phase
$()_0$	value at equilibrium

1. Introduction

It is well-known that the absorption of surface-active agents, i.e., surfactants drastically retards interfacial mass transfer. For example, Frew (1997) conducted laboratory experiments under an identical wind velocity with seawaters sampled at different areas. They showed that the reduction rate of the mass transfer rate was as high as 90% in the case of coastal waters containing the highest level of surfactants. This suggests that the unique relationship between the wind velocity and the mass transfer rate, which is usually assumed in estimating the atmosphere-ocean gas flux, is unlikely to exist for natural waters.

In natural waters, surfactants are commonly present due to marine exudates, excretion and degradation products of phytoplankton, machine lubricants and so forth. In general, surfactants influence air-water gas exchange through static and dynamic mechanisms. The static effect represents the additional resistance to mass transfer due to physical barrier provided by a surfactant layer. This effect is considered to be minor in the real ocean (Frew, 1997; Donelan & Wanninkhof, 2002). In contrast, the dynamic effect is pronounced even at a slightly contaminated interface. The viscoelastic properties of a contaminated interface modify interfacial boundary conditions so as to oppose eddy motions close to the interface (Davies, 1966). As a result, free surface turbulence and associated gas exchange are strongly damped. In the present study, we focus on the hydrodynamic effect, which is also referred to Marangoni effect.

Up to now, numerous studies of gas transfer across clean and contaminated air-water interfaces have been carried out in stirred vessels and wind-wave facilities, e.g., Asher and Pankow (1986) and Jähne et al. (1987). In these studies, a common trend has been observed. Specifically, the mass transfer rate Q increases only slowly below a critical wind velocity, while it suddenly increases beyond the critical wind velocity. It was also confirmed that the Schmidt number dependence of Q switches from $Q \propto Sc^{-0.7}$ to $Q \propto Sc^{-0.5}$ above the critical wind velocity (Jähne et al., 1987). Since the Schmidt number of slightly soluble gases such as CO_2 is generally high ($Sc = O(10^3)$), the transition of the mass transfer mode causes a tenfold difference in the mass transfer rate.

So far, most researchers have been attributing the transition of the mass transfer mode to capillary-gravity waves, which start to grow beyond the critical wind

velocity. In contrast, Jähne et al. (1987) argued that the change in the Schmidt number dependency of the mass transfer rate indicates a change in the transport mechanism. It should be a transition from a rigid to a free surface regime rather than from a smooth to a rough regime. Actually, direct measurement of concentration fluctuations close to an interface (Lee et al., 1980; Asher and Pankow, 1986) indicate that surface renewal eddies are retarded due to surface contamination, and therefore the concentration fluctuations are drastically decreased inside a viscous sublayer. Despite considerable researches, interaction between underlying eddies and a contaminated interface, and associated turbulent mass transfer have not been well understood due to various obstacles in simultaneous measurement of the velocity and concentration fields close to a free surface.

Numerical simulations are quite useful in clarifying such microscopic transport phenomena close to an interface. For example, Tsai and Yue (1995) studied laminar interactions between a contaminated free surface and a vortical flow below. Shen et al. (2004) studied turbulence structures close to a contaminated shear-free surface and observed drastic damping of up- and downwelling motions, which play a critical role in near-surface turbulent transport. Handler et al. (2003) clarified the relationship between an interfacial thermal field and underlying free surface turbulence close to a contaminated interface by direct numerical simulations (DNS). However, no numerical study focuses on the transition of the mass transfer mode so far.

In the present study, we conduct numerical simulation of high Schmidt number turbulent mass transfer across clean, contaminated and solid interfaces in order to understand how an interfacial dynamical condition influences the interfacial mass transfer. We pay particular attention to the transition mechanisms of the turbulent mass transfer mode by systematically changing the Marangoni number representing a degree of surface contamination. We will proceed as follows. First, we show fundamental statistics inside a concentration boundary layer close to clean, contaminated and solid interfaces. Then, we study the transition mechanisms of the turbulent mass transfer mode at a contaminated interface. Finally, a critical parameter for the transition is discussed.

2. Computational Model and Numerical Method

2.1 Numerical conditions

In this study, we consider a countercurrent air-water flow driven by constant pressure gradient as shown in Fig. 1, where x , y and z are the streamwise, interface-normal and spanwise directions, respectively. This configuration is advantageous for highlighting the effects of interfacial shear stress, since the free-slip boundary condition can be imposed at the bottom boundary to minimize its effects. It should be also noted that this configuration is nearly equivalent to a co-current air-water flow in which a coordinate system moves at the same speed as that of the interface, because the mean pressure gradient plays only a minor role compared with the interfacial shear in the near-interface region.

The governing equations of the velocity field are the incompressible Navier-Stokes and the continuity equations:

$$\frac{\partial u_i}{\partial t} + \frac{\partial(u_j u_i)}{\partial x_j} = -\frac{\partial p}{\partial x_i} + \frac{1}{Re_\tau} \frac{\partial^2 u_i}{\partial x_j \partial x_j}, \quad (1)$$

$$\frac{\partial u_i}{\partial x_i} = 0. \quad (2)$$

Here, the velocity u_i and the coordinate x_i are non-dimensionalized by the interfacial friction velocity u_τ^* and the depth δ^* in each phase. The friction velocity is defined as

$u_\tau^* = \sqrt{\tau^* / \rho^*}$, where τ is the interfacial shear stress and ρ is the density of each phase. A

value with an asterisk represents a dimensional value throughout this article. The Reynolds numbers based on u_τ^* and δ^* are $Re_{\tau w} = Re_{\tau a} = 150$, which approximately correspond to an air-water flow at a wind speed of 2 m/s at $y_a^* = \delta^*$ and δ^* of 4 cm under the standard condition where the temperature is 298.15 K and the pressure is 10^5 Pa. Variables with subscripts of a and w represent values in the air and water phases, respectively. The density ratio of water and air is $\rho_w^* / \rho_a^* = 841$.

The computational periods are $2.5\pi\delta^*$ and $\pi\delta^*$ in the x and z directions, respectively. We confirmed that the extension of the computational domain does not affect the velocity and concentration statistics discussed here. A free-slip condition is

imposed at the outer boundaries in both phases. A pseudo-spectral method is applied for spatial discretization. 64 x 64 Fourier modes and 128 Chebyshev polynomials are used in the horizontal and normal directions, respectively. The grid resolution employed for the velocity field is listed in Table 1. Computation with doubled modes in each direction was conducted to ensure that the present grid system is fine enough to resolve all essential scales of the velocity field. For time integration, the second-order Adams-Bashforth scheme is adopted for the advection terms, while the Crank-Nicolson scheme for the viscous terms.

2.2 Hybrid DNS/LES Scheme

The transport equation of solute concentration is given by:

$$\frac{\partial c}{\partial t} + \frac{\partial(u_j c)}{\partial x_j} = \frac{1}{Sc Re_\tau} \frac{\partial^2 c}{\partial x_j \partial x_j}, \quad (3)$$

where, the concentration c is normalized by the concentration difference ΔC^* between the interface and the bottom boundary in the water phase. In general, except for highly soluble or reactive gases, the most mass transfer resistance exists on the water side (Jähne and Haubecker, 1998). In addition, Hasegawa and Kasagi (2008) showed that air-water coupling effects of the concentration fields are insignificant in the present configuration. Hence, we solve the concentration field only in the water phase under constant concentration conditions, i.e., $c = 1.0$ and 0 at the interface and the bottom boundary, respectively. The Schmidt number $Sc = \nu^* / D^*$ is defined by the kinematic viscosity ν^* and the molecular diffusivity D^* of a solute. In the present study, Sc is changed as 1.0 and 100. In the case of $Sc = 1.0$, the same numerical scheme and grid system as those for the velocity field are used (see, Table 1).

For resolving a thin concentration boundary layer at $Sc = 100$, we apply a hybrid DNS/LES scheme, which employs DNS with high-resolution grids within the near-surface region, while large-eddy simulation (LES) with coarser grids in the outer layer (Hasegawa and Kasagi, 2007). By employing such a solution-adaptive scheme, we can calculate the high Schmidt number concentration field with reasonable cost, while maintaining accuracy near the interface. In order to connect the DNS and LES regions

smoothly, we provide a switching region between them, where the subgrid-scalar flux is gradually imposed with the distance from the interface. A pseudo-spectral method is adopted in the horizontal directions, while a finite-volume method in the normal direction. The details of the hybrid DNS/LES scheme can be found in Hasegawa and Kasagi (2007).

In employing the hybrid DNS/LES, we note the following issues.

1. Depth of DNS region δ_{DNS}
2. Grid resolution in DNS region
3. Subgrid-scale model in LES region

Hasegawa and Kasagi (2007) conducted thorough verification on these issues at two limiting regimes of a clean free surface and a solid wall. Specifically, the depth of the DNS region was changed from $\delta_{\text{DNS}}^+ = 11.3$ to 22.8. The numbers of Fourier modes employed in the x and z directions were increased 192 to 512, while the number of grids in the y direction in the DNS and switching regions was changed from 49 to 109. From these calculations, it was shown that $\delta_{\text{DNS}}^+ = 11.3$ and 192×192 Fourier modes in the horizontal directions are sufficient to obtain the fundamental concentration statistics. The depth and the grid resolution in the DNS, LES and switching regions are listed in Table 1. The dynamic Smagorinsky model (Germano et al., 1991) is used in the LES region. Considering that a contaminated interface generally falls between clean and solid interfaces, we adopt the same grid system for contaminated interfaces.

2.3 Interfacial Boundary Conditions

Since we focus on effects of an interfacial dynamical condition on the mass transfer, the interface is assumed to be flat for simplicity, i.e., $v_w = v_a = 0$. The resultant interfacial boundary conditions for the velocity field are the continuity of velocity components and the balance of the shear stress and the surface tension in the tangential directions. They are written in dimensionless forms as:

$$u_{wj} = \sqrt{\frac{\rho_w^*}{\rho_a^*}} u_{aj} \quad (4)$$

$$\frac{1}{Re_{\tau_w}} \frac{\partial u_{wj}}{\partial x_2} = \frac{1}{Re_{\tau_a}} \frac{\partial u_{aj}}{\partial x_2} - \frac{1}{We} \frac{\partial \sigma}{\partial x_j} \quad (5)$$

Here, $j = 1$ or 3 . The surface tension σ is normalized by the equilibrium surface tension σ_0^* . The Weber number is defined by $We = \tau^* \delta^* / \sigma_0^*$.

Generally, a contaminated interface exhibits complex stress response to compressional and dilational straining (Frew, 1997). For simplicity, we assume the following linear relationship between the surface tension σ and the surfactant concentration γ (Handler et al., 2003; Shen et al., 2004):

$$\sigma - 1 = Ma(1 - \gamma). \quad (6)$$

Here, γ is normalized by the equilibrium concentration γ_0^* . It should be noted that Eq. (6) is valid for a highly contaminated interface in which $\gamma' \ll 1$. The Marangoni number is defined by $Ma = -(\gamma_0^* / \sigma_0^*) \cdot (d\sigma^* / d\gamma^*)|_{\gamma=1}$. By substituting Eq. (6), the

interfacial boundary condition (5) can be rewritten as:

$$\frac{1}{Re_{\tau_w}} \frac{\partial u_{wj}}{\partial x_2} = \frac{1}{Re_{\tau_a}} \frac{\partial u_{aj}}{\partial x_2} + \frac{Ma}{We} \frac{\partial \gamma}{\partial x_j}. \quad (7)$$

In the present study, the Weber number is kept constant, i.e., $We = 9.0 \times 10^{-4}$, while the Marangoni number is systematically changed as $Ma = 0$ (Clean), 1.0×10^{-3} (Case 1), 1.0×10^{-2} (Case 2) and 1.0×10^{-1} (Case 3). Note that $Ma = 0$ corresponds to a clean interface. In addition to the four cases, a solid surface is also considered for comparison by imposing a no-slip condition at the interface instead of Eqs. (4) and (7). All computational conditions are summarized in Table 2.

The transport equation of an insoluble surfactant gives rise to:

$$\frac{\partial \gamma}{\partial t} + \frac{\partial(u_w \gamma)}{\partial x} + \frac{\partial(w_w \gamma)}{\partial z} = \frac{1}{Sc_\gamma Re_{\tau_w}} \left(\frac{\partial^2 \gamma}{\partial x^2} + \frac{\partial^2 \gamma}{\partial z^2} \right). \quad (8)$$

Note that the total amount of the surfactant on the interface is always conserved. The Schmidt number of the surfactant is $Sc_\gamma = 1.0$ in all cases.

The whole computation proceeds as follows. First, the governing equations (1, 2) for the velocity fields in the air and water phases are solved under the coupled

interfacial boundary conditions (4) and (7). Similarly, the transport equation (3) of the solute concentration is solved in the water phase. The obtained velocity field at the interface is used for solving the surfactant transport equation (8). The resultant surfactant concentration is assigned to the interfacial velocity boundary condition (7) in the next step. The time step in the shear unit is $t_w^+ = 0.018$ in all calculations so that the Courant conditions for solving the velocity and concentration fields should be met. After the velocity and concentration fields reached the statistically steady state, we integrated the set of the governing equations up to $t_w^+ = 2000$ in order to obtain the statistics shown below.

3. Results

3.1 Velocity Field

Since the interface is dynamically similar to a solid surface for the air flow due to large density ratio between water and air (Lombardi, et al., 1996), and the total gas exchange is determined by the microscopic transport phenomena on the water side, we focus on the flow statistics on the water side. The mean velocity profiles in the water phase relative to the interfacial velocity are shown in Fig. 2. Although the logarithmic region with the same slope is observed, a gap in the mean velocity profiles exists between a clean interface and a solid wall. With increasing the Marangoni number, thickness of the viscous sublayer is gradually increased, and eventually the profile converges to that near a solid wall.

The velocity fluctuations plotted in Fig. 3 exhibit distinct features close to the contaminated interface. Specifically, the streamwise and spanwise velocity fluctuations are kept almost unchanged, while only the normal velocity fluctuation is damped drastically with increasing the Marangoni number. This indicates that the velocity field near a highly contaminated interface is essentially different from that near a solid surface.

In order to clarify the surfactant effects on the flow field, the interfacial velocity vector is decomposed into irrotational and solenoidal components by applying Helmholtz's theorem as illustrated in Fig. 4. Once $\partial v / \partial y$ and ω_y at the interface are calculated, the two components can be obtained by solving the following set of

equations:

$$\left\{ \begin{array}{l} \frac{\partial u_{IR}}{\partial x} + \frac{\partial w_{IR}}{\partial z} = -\frac{\partial v}{\partial y} \Big|_{y=0} \\ \frac{\partial u_{IR}}{\partial z} - \frac{\partial w_{IR}}{\partial x} = 0 \end{array} \right., \quad \left\{ \begin{array}{l} \frac{\partial u_{SL}}{\partial x} + \frac{\partial w_{SL}}{\partial z} = 0 \\ \frac{\partial u_{SL}}{\partial z} - \frac{\partial w_{SL}}{\partial x} = -\omega_y \Big|_{y=0} \end{array} \right. . \quad (9)$$

Here, the vectors with subscripts of *IR* and *SL* represent irrotational and solenoidal components, respectively. The partial kinetic energy k_{IR} and k_{SL} held by the two components, and their relative contributions to the total kinetic energy $k_{Total} = k_{IR} + k_{SL}$ are listed in Table 2. A distinctive feature of a contaminated interface is selective damping of the irrotational motion. Hence, the contaminated interface behaves like a no-slip boundary for the irrotational motion, while a free-slip boundary for the solenoidal motion. This is reasonable because the additional shear stress due to a surfactant appears as gradient of the surfactant concentration γ in Eq. (7). Since $\nabla \times (\nabla \gamma) = 0$, a surfactant does not directly produce the interface-normal vorticity.

The irrotational motion is directly linked to the surface divergence β , which is defined by two dimensional divergence of the tangential velocity on the interface.

$$\beta = \left(\frac{\partial u}{\partial x} + \frac{\partial w}{\partial z} \right)_{y=0} = - \left(\frac{\partial v}{\partial y} \right)_{y=0} . \quad (10)$$

Note that the surface divergence is equivalent to the interface-normal derivative of v due to the continuity. The drastic damping of the surface divergence is also observed in the numerical study of a shear-free interface by Shen et al. (2004).

Since v' plays a critical role in the mass transfer, the surface divergence has been considered as a key parameter for predicting the mass transfer. In fact, recent experiments indicate that statistical properties of the surface divergence can be related to the mass transfer rate regardless of a mode of turbulence generation, surface contamination and interfacial deformation (Law and Khoo, 2002; McKenna and McGillis, 2004; Turney et al., 2005). The frequency spectra W_β of the surface divergence at clean and contaminated interfaces are shown in Fig. 5. In calculating W_β , the time traces of the local surface divergence on 64 x 64 uniform grids at the interface were stored per $t^+ = 0.3$ for a period of $t^+ = 3000$. Before applying FFT, we multiplied the time-series data by a window function with a long constant value sandwiched between two short cosine bells (Bingham, et al., 1967) in order to avoid spreading of spectra due to limited sampling time. It is found that low-frequency fluctuations are

drastically decreased with increasing the Marangoni number. As will be discussed in Sec. 3, this leads to drastic change of turbulent mass transfer mode, even though the irrotational motions contain only a small fraction of the total kinetic energy (see, Table 2.)

3.2 Concentration Field

The mean concentration profiles near the clean, contaminated and solid interfaces at $Sc = 100$ are presented in Fig. 6. The abscissa is the distance from the interface in the shear unit. The ordinate is the mean concentration relative to the interfacial concentration non-dimensionalized by the friction concentration. Here, the friction concentration is defined as $c_\tau^* = Q^* / u_\tau^*$, where Q^* is the mean interfacial mass flux. A distinct difference between the clean and solid interfaces can be found. With increasing the Marangoni number, the mean concentration approaches to that near the solid interface in a similar way to the mean velocity profile shown in Fig. 2.

The thickness δ_c of the diffusive sublayer, in which $C^+ = Scy^+$ is satisfied within deviation of 5 %, is listed in Table 3. Magnaudet and Calmet (2006) showed that δ_c is scaled by $\delta_c^* / L^* \approx 2.0 Re_T^{-3/4} Sc^{-1/2}$, where L is the integral length scale and Re_T is the turbulent Reynolds number based on L and the macroscopic velocity scale u_T determined by the averaged kinetic energy at $y = L$. By assuming $L^+ = 30$ and $u_T^+ = 1.8$, which correspond to the typical diameter of quasi-streamwise vortices close to the interface and the velocity scale determined from the interfacial kinetic energy, δ_c is estimated as $\delta_c^+ \approx 3.0 Sc^{-1/2}$. This leads to $\delta_c^+ \approx 3.0$ and 0.3 at $Sc = 1.0$ and 100 , respectively. Although the above correlation was developed at a shear-free interface, this is found to predict the present result at a clean sheared interface well (see, Table 3). With increasing the Marangoni number, however, δ_c^+ becomes thicker, and approaches the value at a solid wall. Schwertfirm and Manhart (2007) argued that δ_c varies as $\delta_c^+ \propto Sc^{-0.29}$ at a solid wall. In order to show the Schmidt number dependency of δ_c^+ , the Schmidt number exponent n , i.e., $n = \log_{100} \left\{ \delta_c^+(Sc = 100) / \delta_c^+(Sc = 1.0) \right\}$, is listed in Table 3. The exponent is close to -0.5 at clean and slightly contaminated (Case1) interfaces, while $n \sim -0.3$ at highly contaminated interfaces (Cases 2 and 3). These results suggest the scaling law of δ_c is changed from that near a free surface to that near a solid surface. This trend is consistent with the change of mass transfer mode discussed

in Sec. 3.3.

The concentration fluctuation c_{rms} at $Sc = 100$, which is normalized by the difference ΔC_B between the interfacial and bulk concentrations, is shown in Fig. 7. Although a slight bump is observed at the connection plane between the switching and LES regions due to rapid change of numerical resolution, it was shown that this does not affect the profile inside the DNS region (Hasegawa and Kasagi, 2007). With increasing the Marangoni number, the peak value is drastically decreased and the peak location y_p^+ moves further from the interface, i.e., $y_p^+ = 1.0, 1.2$ and 2.2 for clean and contaminated interfaces (Cases 1 and 2), respectively. These results qualitatively agree with direct observation of concentration fluctuations close to clean and contaminated air-water interfaces by Asher and Pankow (1989). They applied the laser-induced fluorescence (LIF) technique to observe CO_2 concentration fluctuations caused by air-water gas transfer, and observed 40 % decrease of the fluorescence fluctuations close to a contaminated interface. The concentration fluctuations at high Marangoni numbers (Cases 2 and 3) are slightly lower than that near a solid surface. This may be attributed to the large tangential velocity fluctuations at a contaminated interface (see, Fig. 3).

3.3 Transition of Turbulent Mass Transfer Mode

The global mass transfer rate Q^+ in the water phase is defined by:

$$Q^+ = \frac{Q^*}{u_\tau^* (C_I^* - C_B^*)} = \frac{1}{\Delta C_B^+}. \quad (11)$$

Here, C_I^* and C_B^* are the mean concentrations at the interface and the bulk, respectively, while $\Delta C_B^* = C_I^* - C_B^*$. The mass transfer rates at $Sc = 1.0$ and 100 in all cases are plotted in Fig. 8. With increasing the Marangoni number, the mass transfer rate is drastically decreased, and eventually converges to the value on a solid surface. Surface contamination has a profound effect at the high Schmidt number, since the most resistance to mass transfer lies in a thinner layer beneath the interface. Specifically, the mass transfer rate is decreased by 60 % at $Sc = 100$, while only 25 % at $Sc = 1.0$. The mass transfer rates in all cases are also listed in Table 2. Jähne et al. (1987) compiled experimental data for $Sc \sim O(10^2)$ at two limiting regimes of clean and highly contaminated interfaces. They showed that the mass transfer rate is correlated as $Q^+ = 0.11Sc_w^{-0.5}$ and $0.073Sc_w^{-0.7}$ for clean and highly contaminated interfaces, respectively. Banerjee et al. (2004) conducted DNS of turbulent mass transfer at a

deformable sheared interface without surface contamination. These data are also plotted in Fig. 8. As a whole, the present results agree well with the previous data.

It is known that the Schmidt number dependency of the mass transfer rate at a solid surface changes around $Sc = 10$. Specifically, the DNS data obtained by Na et al. (1999) leads to $Q^+ = 0.0509Sc_w^{-0.546}$ for Sc up to 10. In contrast, mass transfer measurements with electrochemical techniques by Shaw and Hanratty (1977) indicate $Q^+ = 0.0889Sc_w^{-0.704}$ for $700 < Sc < 37000$. Hence, the Schmidt number dependency cannot be determined with only two data points available in the present study. Nonetheless, the convergence of the mass transfer rate at a highly contaminated interface to the value at a solid interface indicates that the turbulent mass transfer mechanism switches from that near a free surface to that near a solid surface.

The change of the turbulent transfer mode clearly appears in the limiting behavior of an eddy diffusivity E_d as shown in Fig. 9. Considering the limiting behavior of velocity and concentration fluctuations, the eddy diffusivity varies as $E_d^+ \propto y^{+2}$ and $E_d^+ \propto y^{+3}$ in the immediate vicinity of free and solid interfaces, respectively (Hasegawa and Kasagi, 2007). In the case of a clean or slightly contaminated interface (Case 1), E_d^+ is proportional to y^{+2} . With increasing the Marangoni number, the region in which $E_d^+ \propto y^{+2}$ decreases and lies in the diffusive sublayer, where turbulent transport is not significant. Eventually, E_d^+ converges to the data at a solid surface. These results are consistent with the mass transfer rates shown in Fig. 8.

It is known that the regions where $E_d^+ \propto y^{+3}$ holds near a solid interface always lies in the diffusive sublayer so that E_d is better represented by $E_d^+ = 0.000463y^{+3.38}$ over the concentration boundary layer (Shaw and Haratty, 1977; Hasegawa and Kasagi, 2007). The present data at highly contaminated and solid interfaces agree with the correlation plotted in Fig. 9. The increase of the slope of E_d^+ , i.e., $E_d \propto y^n, n > 3$, is also observed near a deformable air-water interface (Lakehal et al., 2003).

4. Transition Mechanism of Turbulence Mass Transfer Mode

4.1 One-dimensional Advection-diffusion Equation

Due to a thin concentration boundary layer at the high Schmidt number, the transport equation (3) of the solute concentration can be simplified to (McCready and

Hanratty, 1984):

$$\frac{\partial c}{\partial t^+} + v^+ \frac{\partial c}{\partial y} = \frac{1}{Sc} \frac{\partial^2 c}{\partial y^{+2}}. \quad (12)$$

Since the interfacial shear stress governs the mass transfer in the specific situation being considered, the velocity and the length are non-dimensionalized by the shear units on the water side, while the concentration is normalized by ΔC_B^* .

In general, the normal velocity fluctuation v' close to an interface can be represented by Taylor series expansion about the interface as:

$$v^+(y^+, t^+) = \left(\frac{\partial v^+}{\partial y^+} \right)_{y^+=0} y^+ + \frac{1}{2} \left(\frac{\partial^2 v^+}{\partial y^{+2}} \right)_{y^+=0} y^{+2} + \dots. \quad (13)$$

Truncating to the first term, v' inside a concentration boundary layer at a free surface can be expressed by the surface divergence β as $v^+(y^+, t^+) = -\beta^+(t^+)y^+$. In contrast, β should be zero at a solid surface due to a no-slip condition, so that v' varies as $v^+ \propto y^{+2}$. It should be noted that the fundamental difference between free and solid surfaces in terms of the mass transfer stems from the difference in the asymptotic behavior of v' toward the interface (Hasegawa and Kasagi, 2007).

Hasegawa and Kasagi (2005, 2008) considered a single sinusoidal wave for β , i.e., $\beta^+(t) = \sqrt{2}\beta_0^+ \cos(\omega_0^+ t)$. By introducing a new coordinate $Y = \sqrt{Sc\omega_0^+} y^+$ and a time-scale $T = \omega_0^+ t$, the Schmidt number disappears from Eq. (12) and the only remaining parameter is β_0 / ω_0 .

$$\frac{\partial c}{\partial T} - \sqrt{2} \frac{\beta_0^+}{\omega_0^+} \cos(T) \cdot Y \cdot \frac{\partial c}{\partial Y} = \frac{\partial^2 c}{\partial Y^2}. \quad (14)$$

Based on an order-of-magnitude estimate, it was shown that the fluctuating surface divergence contributes to the mass transfer only when $\beta_0 / \omega_0 \gg 1$, and if this is the case, the local mass transfer rate q^+ is determined by the balance between the advection and diffusion terms in Eq. (14). As a result, q^+ can be estimated by the following Chan and Scriven's stagnation flow model (1970).

$$q^+ = \frac{q^*}{u_\tau^* \Delta C_B^*} = \sqrt{\frac{2\beta^+}{\pi \cdot Sc}}. \quad (15)$$

In Fig. 10, the contributions of the local surface divergence β^+ to the local mass transfer rate q^+ at clean and contaminated interfaces are shown. The contour value

represents the product of the local mass flux q^+ and the joint probability density function of β^+ and q^+ , so that the integral of the contour values over the whole β^+ - q^+ plane is identical to the total interfacial mass flux. The data at a clean interface is quoted from our previous work (Hasegawa and Kasagi, 2008). The prediction by Eq. (15) and the global mass transfer rate Q^+ at a solid surface are depicted as solid and dotted lines, respectively. At a clean interface, q^+ agrees well with Eq. (15). In contrast, with increasing Ma , the correlation between q^+ and β^+ rapidly deteriorates, and eventually, the contour converges around the data at a solid surface in Cases 2 and 3. These results indicate that the vanishing contribution of the surface divergence to the mass transfer is a primary reason for the transition of the mass transfer mode. When the contribution of the surface divergence is negligible, the second term of Eq. (13) becomes dominant in the mass transfer. This regime is essentially the same as a solid surface in terms of the mass transfer.

4. 2 Surface Divergence Model

McCready et al. (1986) carried out numerical simulation of a two-dimensional advection-diffusion equation close to a free surface. They concluded that the global mass transfer rate Q is correlated with the surface divergence β as:

$$Q^+ = A \sqrt{\frac{\beta_{rms}^+}{Sc}}. \quad (16)$$

Here, $A \sim O(1)$ is a dimensionless proportional constant. For a sheared interface, Eq. (16) with $A = 0.45$ appears to predict the mass transfer rate reasonably (Banerjee et al., 2004; Turney et al., 2005). Hasegawa and Kasagi (2008) numerically solved Eq. (14) and obtained $A = 0.4$. In Fig. 11, the mass transfer rates obtained in the present study are plotted with open symbols as a function of $\sqrt{\beta_{rms}^+}$. Eq. (16) with $A = 0.4$ is also depicted as a solid line. At a clean interface, the mass transfer rate shows good agreement with Eq. (16). At a slightly contaminated interface (Case 1), however, the mass transfer rate rapidly decreases and deviates from Eq. (16). For highly contaminated interfaces (Cases 2 and 3), the mass transfer rate is almost independent of the surface divergence and converges to the data at the solid interface. These facts indicate that the original surface divergence model (16) is not applicable to a contaminated interface considered here.

As discussed in the previous section, the theoretical support of the surface divergence model (16) comes from the Chan and Scriven's stagnation flow model (15), which relates the local mass transfer rate to the surface divergence. With increasing Ma , however, the local mass transfer rate is less correlated to the surface divergence as shown in Figs. 10 (a-d). Consequently, the surface divergence model fails at a contaminated interface.

Hasegawa and Kasagi (2005, 2008) analyzed Eq. (12), and showed that the solution undergoes sudden transition around $\beta_0 / \omega_0 \sim 1$. Specifically, when $\beta_0 / \omega_0 \gg 1$, the correlation between the local mass transfer rate and the surface divergence is kept high, and the surface divergence model (16) holds fairly well. In contrast, when $\beta_0 / \omega_0 \ll 1$, the correlation between the local mass flux and the surface divergence drastically deteriorates, and therefore the mass transfer rate rapidly decreases. These results indicate that in order for the fluctuating surface divergence to contribute to the mass transfer, its frequency ω_0 need to be sufficiently smaller than its intensity β_0 . Hereafter, we will refer to the surface divergence contributing to the mass transfer as the effective surface divergence. Note that $1 / \beta_0$ represent a transient response time-scale of the concentration boundary layer, while $1 / \omega_0$ is the renewal time-scale (Hasegawa and Kasagi, 2005, 2008). Therefore, β_0 / ω_0 is a dimensionless parameter, which characterizes the concentration field close to an interface.

In view of these facts, we calculate the ratio between typical intensity and frequency of the fluctuating surface divergence at clean and contaminated interfaces. β_{rms} is chosen for the typical intensity of the fluctuating surface divergence. For the typical frequency, we employ the mean frequency ω_m (McCready et al., 1986) given by the following equation:

$$\omega_m = \frac{\int_0^\infty \omega' W_\beta(\omega') d\omega'}{\int_0^\infty W_\beta(\omega') d\omega'}. \quad (17)$$

The ratio of β_{rms} and ω_m is listed in Table 2. Since lower-frequency fluctuations of the surface divergence are damped due to surface contamination (see, Fig. 5), ω_m is increased with increasing Ma , i.e., $\omega_m^+ = 0.22, 0.36, 0.57$ and 1.4 in Clean and Cases 1-3, respectively. In contrast, β_{rms} vanishes with increasing Ma . As a result, β_{rms} / ω_m drastically decreases with increasing Ma . These results suggest that the surface divergence at highly contaminated interfaces is no longer effective in the mass transfer.

This is consistent with the deterioration of the correlation between β^+ on q^+ in Fig. 10.

The above results stress the importance of quantifying the effective surface divergence for prediction of the mass transfer rate at a contaminated interface. Hasegawa and Kasagi (2005) developed a method to extract the effective surface divergence from time-series data of the surface divergence. In the present study, we propose another simpler method to estimate the effective surface divergence from a frequency spectrum. In general, the energy of the surface divergence contained below a certain frequency ω can be estimated as $\int_0^\omega W_\beta(\omega')d\omega'$. Hence, in order for the surface divergence to contribute to the mass transfer, its frequency should be smaller than the following critical frequency ω_c :

$$\omega_c = B^{-1} \sqrt{\int_0^{\omega_c} W_\beta(\omega')d\omega'}. \quad (18)$$

Here, $B \sim O(1)$ is the dimensionless proportional constant. It is found that $B = 0.25$ provides reasonable prediction in the present study. We estimate the effective surface divergence β_E from the energy which lies below the critical frequency ω_c as:

$$\beta_E = \sqrt{\int_0^{\omega_c} W_\beta(\omega')d\omega'}. \quad (19)$$

Since ω_c^+ decreases with increasing Ma as $\omega_c^+ = 0.19, 0.10, 0.0067$ and 0 , β_E decreases as $\beta_E = 0.047, 0.023, 0.0010$ and 0 for clean and contaminated (Cases 1-3) interfaces. The mass transfer rates at clean and contaminated interfaces are replotted as a function of $\sqrt{\beta_E}$ with solid symbols in Fig. 11. It is found that the mass transfer rate for clean and slightly contaminated (Case 1) interfaces can be predicted fairly well with Eq. (16). At highly contaminated interfaces (Cases 2 and 3), β_E are too small to explain the present data. This means that the interface is more like a solid interface in terms of the mass transfer, so that the mass transfer rate converges to the data at a solid surface.

5. Conclusions

Numerical simulations of high Schmidt number turbulent mass transfer across clean, contaminated and solid interfaces were systematically carried out in order to clarify effects of an interfacial dynamical condition on the interfacial mass transfer. By applying a hybrid DNS/LES scheme to the high Schmidt number concentration field, we could numerically reproduce a transition process of turbulent mass transfer mode

from a free surface to a solid surface for the first time. At a clean interface, the surface divergence plays a critical role in the mass transfer. In contrast, at a contaminated interface, the correlation between the local mass transfer rate and the surface divergence drastically deteriorates, and eventually the mass transfer rate falls down to the value at a solid surface. The transition of the turbulent mass transfer mode can be explained by a one-dimensional advection-diffusion equation. Specifically, the fluctuating surface divergence contributes to the mass transfer only when its frequency is sufficiently lower than its intensity. In the present study, we developed a method to extract the effective surface divergence from a frequency spectrum. It was shown that the mass transfer rate at a clean or slightly contaminated interface is correlated to the effective surface divergence. At a highly contaminated interface, the surface divergence fluctuations at low frequencies are drastically damped, so that the effective surface divergence becomes vanishingly small. Consequently, the turbulent mass transfer mode switches to that near a solid surface. We showed that the ratio of the intensity and the mean frequency of the fluctuating surface divergence can be used as a criterion for the transition of the mass transfer mode.

The present results shed light on the importance of frequency range of the surface divergence, as well as its intensity in predicting the interfacial turbulent mass transfer. How to predict the frequency spectrum of the surface divergence at a contaminated interface is still open question. Furthermore, in a real air-water interface, onset of capillary-small gravity waves should influence turbulent structures close to an interface. Clarification of the surface deformation effects on the frequency spectrum of the surface divergence remains to be future work.

Acknowledgement

The present work was partially supported through Grant-in-Aid for Young Scientists (B), 19760131, 2007, and also the 21st Century COE Program, “Mechanical Systems Innovation,” by the Ministry of Education, Culture, Sports, Science and Technology, Japan.

References

- [1] Asher, W. E., and Pankow, J. F., 1986. The interaction of mechanically generated turbulence and interfacial films with a liquid phase controlled gas/liquid transport process, *Tellus* 38B, 305-318
- [2] Asher, W. E., and Pankow, J. F., 1989. Direct observation of concentration fluctuations close to a gas-liquid interface, *Chemical Engineering Science* 44 (6), 1451-1455.
- [3] Banerjee, S., Lakehal, D. and Fulgosi, M., 2004. Surface divergence models for scalar exchange between turbulent streams, *International Journal of Multiphase Flow* 30 (7-8), 963-977.
- [4] Bingham, C., Godfrey, M. D. and Tukey, J. M., 1967, Modern techniques of power spectrum estimation, *IEEE Transactions on Audio and Electroacoustics* AU-15 (2), 56-66.
- [5] Chan, W. C., and Scriven, L. E., 1970. Absorption into irrotational stagnation flow, *Industrial Eng. Chem. Fund.* 9 (1), 114-120.
- [6] Davies, J. T., 1966. The effects of surface films in damping eddies at a free surface of a turbulent liquid, *Proc. R. Soc. London*, A290, 515-526.
- [7] Donelan, M. A., and Wanninkhof, R., 2002. Gas Transfer at Water Surfaces – Concepts and issues, *Gas Transfer at Water Surfaces* (ed. Donelan, M. A., Drennan, W. M., Saltzman, E. W., & Wanninkhof, R.), 1-10, American Geophysical Union, Washington.
- [8] Frew, N. M., 1997. The role of organic films in air-sea gas exchange, *The Sea Surface and Global Change* (ed. Liss, P. S., and Duce, R. A.), 121-172, Cambridge University Press, New York.
- [9] Germano, M., Piomelli, U., Moin, P. and Cabot, W., 1991. A dynamic mixed subgrid scale model and its application to turbulent recirculating flows, *Phys. Fluids* A3, 1760-1765.
- [10] Handler, R. A., Leighton, R. I., Smith, G. B., and Nagaosa, R., 2003. Surfactant effects on passive scalar transport in a fully developed turbulent flow. *Int. J. Heat Mass Trans.* 46 (12), 2219-2238.
- [11] Hasegawa, Y. and Kasagi, N., 2005. Turbulent Mass Transfer Mechanism across a Contaminated Air-Water Interface. *Proceedings of Fourth International*

Symposium on Turbulent Shear Flow, 971-976.

- [12] Hasegawa, Y. and Kasagi, N., 2007. Effects of Interfacial Boundary Condition on Turbulent Mass Transfer at High Schmidt Numbers, *Int. J. Heat Fluid Flow*, Vol. 28, No. 6, 1192-1203.
- [13] Hasegawa, Y. and Kasagi, N., 2008. Hybrid DNS/LES of High Schmidt Number Mass Transfer Across Turbulent Air-Water Interface, *Int. J. Heat Mass Trans.*, submitted.
- [14] Jähne, B., Münnich, K. O., Böisinger, R., Dutzi, A., Huber, W., and Libner, P., 1987. On the Parameters Influencing Air-Water Gas Exchange, *J. Geophys. Res.* Vol. 92, No. C2, 1937-1949.
- [15] Jähne, B., and Haubecker, H., 1998. Air-Water Gas Exchange, *Annual Review of Fluid Mechanics* Vol. 30, pp. 443-468.
- [16] Lakehal, D., Fulgosi, M., Yadigaroglu, G., and Banerjee, S., 2003. Direct numerical simulation of turbulent heat transfer across a mobile, sheared gas-liquid interface, *Journal of Heat Transfer Transactions of the ASME* 125 (6), pp. 1129-1139.
- [17] Law, C. N. S., and Khoo, B. C., 2002. Transport across a turbulent air-water interface, *AIChE Journal* 48 (9), 1856-1868.
- [18] Lee, Y. H., Tsao, G. T., and Wankat, P. C., 1980. Hydrodynamic Effect of Surfactants on Gas-Liquid Oxygen Transfer, *AIChE Journal* 26 (6), 1008-1012.
- [19] Lombardi, P., De Angelis V. and Banerjee, S., 1996. Direct numerical simulation of near-interface turbulence in coupled gas-liquid flow, *Phys. Fluids* 8, 1643-1665.
- [20] Magnaudet, J. and Calmet I., 2006. Turbulent mass transfer through a flat shear-free surface, *Journal of Fluid Mechanics* Vol. 533, 155-185.
- [21] McCready, M. J. and Hanratty, T. J., 1984. Concentration Fluctuations close to a Gas-Liquid Interface. *A.I.Ch.E. Journal* 30 (5), 816-817.
- [22] McCready, M. J., Vassiliadou, E., and Hanratty, T. J., 1986. Computer Simulation of Turbulent Mass Transfer at a Mobile Interface. *A.I.Ch.E. Journal* 32 (7), 1108-1115.
- [23] McKenna, S. P. and McGillis, W. R., 2004. The role of free-surface turbulence and surfactants in air-water gas transfer, *Int. J. Heat Mass Trans.* 47 (3), 539-553.
- [24] Na, Y., Papavassiliou, D. V., and Hanratty, T. J., 1999. Use of direct numerical simulation to study the effect of Prandtl number on temperature fields,

International Journal of Heat and Fluid Flow 20 (3), 187-195.

- [25] Schwertfirm, F. and Manhart, M., 2007. DNS of passive scalar transport in turbulent channel flow at high Schmidt numbers. International Journal of Heat and Fluid Flow 28 (6), 1204-1214.
- [26] Shaw, D. A. and Hanratty, T. J., 1977. Turbulent mass transfer rates to a wall for large Schmidt numbers, AIChE Journal 23 (1), 28-37.
- [27] Shen, L., Yue, D. K. P. and Triantafyllou G. S., 2004. Effect of Surfactants on Free-Surface Turbulent Flows, J. Fluid Mech. 506, 79-115.
- [28] Tsai, W. T. and Yue, D. K. P., 1995. Effect of Soluble and Insoluble Surfactant on Laminar Interactions of Vortical Flows with a Free Surface, J. Fluid Mech. 289, 315-349.
- [29] Turney, D. E., Smith, W. C. and Banerjee, S., 2005. A measure of near-surface fluid motions that predicts air-water gas transfer in a wide range of conditions, Geophys. Res. Let. 32 (4), L04607.

Figure Captions

- Fig. 1 a) Computational domain and coordinate system, and
b) grid system in hybrid DNS/LES
- Fig. 2 Mean velocity in the water phase relative to the interfacial velocity.
- Fig. 3 Limiting behavior of velocity fluctuations close to the interface.
- Fig. 4 Decomposition of the interfacial velocity vector into
a) solenoidal and b) irrotational components.
- Fig. 5 Frequency spectra of the surface divergence.
- Fig. 6 Mean concentration profiles.
- Fig. 7 Concentration fluctuations.
- Fig. 8 Mass transfer rates as a function of the Schmidt number.
- Fig. 9 Limiting behavior of the eddy diffusivity close to the interface at $Sc = 100$.
- Fig. 10 Contribution of the surface divergence to the interfacial mass flux at $Sc = 100$.
- Fig. 11 Mass transfer rates as a function of
 $\sqrt{\beta_{rms}}$: open symbols and $\sqrt{\beta_{E rms}}$: solid symbols.

Table 1 Number of modes, number of grid points and grid spacings.

		Region	k_x, k_y or N_y, k_z	Δx^+	Δy^+	Δz^+
Velocity (air and water phases) & Scalar ($Sc_w = 1.0$)	DNS	$0 < y^+ < 150$	64, 129, 64	18.4	0.01 ~ 1.23	7.2
Scalar ($Sc_w = 100$)	DNS	$0 < y^+ < 11.3$	192, 34, 192	6.1	0.01 ~ 0.62	2.4
	Switching	$11.3 < y^+ < 21.6$	192, 15, 192	6.1	0.66 ~ 0.85	2.4
	LES	$21.6 < y^+ < 150$	64, 144, 64	18.4	0.01 ~ 0.79	7.2

Table 2 Computational conditions, interfacial kinetic energy k_{SL} and k_{IR} held by solenoidal and irrotational motions, their relative contributions to total kinetic energy $k_{Total} = k_{SL} + k_{IR}$, mass transfer rate K_w , and time-scale ratio β_{rms}/ω_m .

	Ma	We	k_{SL} ($k_{SL} /$ k_{Total})	k_{IR} ($k_{IR} /$ k_{Total})	K_w^+ $Sc_w = 1.0$	K_w^+ $Sc_w = 100$	β_{rms}/ω_m
Clean	0	9.0×10^{-3}	4.9 (0.85)	0.69 (0.15)	6.8×10^{-2}	9.6×10^{-3}	0.27
Case 1	1.0×10^{-3}	9.0×10^{-3}	3.9 (0.90)	0.43 (0.10)	5.9×10^{-2}	5.2×10^{-3}	0.15
Case 2	1.0×10^{-2}	9.0×10^{-3}	3.5 (0.95)	0.18 (0.05)	5.4×10^{-2}	3.9×10^{-3}	4.0×10^{-2}
Case 3	1.0×10^{-1}	9.0×10^{-3}	3.6 (0.992)	0.03 (0.008)	5.1×10^{-2}	3.6×10^{-3}	3.7×10^{-3}
Solid	-	-	0	0	5.5×10^{-2}	3.4×10^{-3}	-

Table 3 Thickness δ_c of the diffusive sublayer and Schmidt number exponent n .

	Clean	Case 1	Case 2	Case 3	Solid
$\delta_c^+ (Sc = 1.0)$	2.8	4.4	6.18	6.18	6.69
$\delta_c^+ (Sc = 100)$	0.25	0.49	1.44	1.44	1.69
$n = \frac{1}{2} \log \left\{ \frac{\delta_c^+ (Sc = 100)}{\delta_c^+ (Sc = 1.0)} \right\}$	-0.52	-0.47	-0.32	-0.32	-0.30

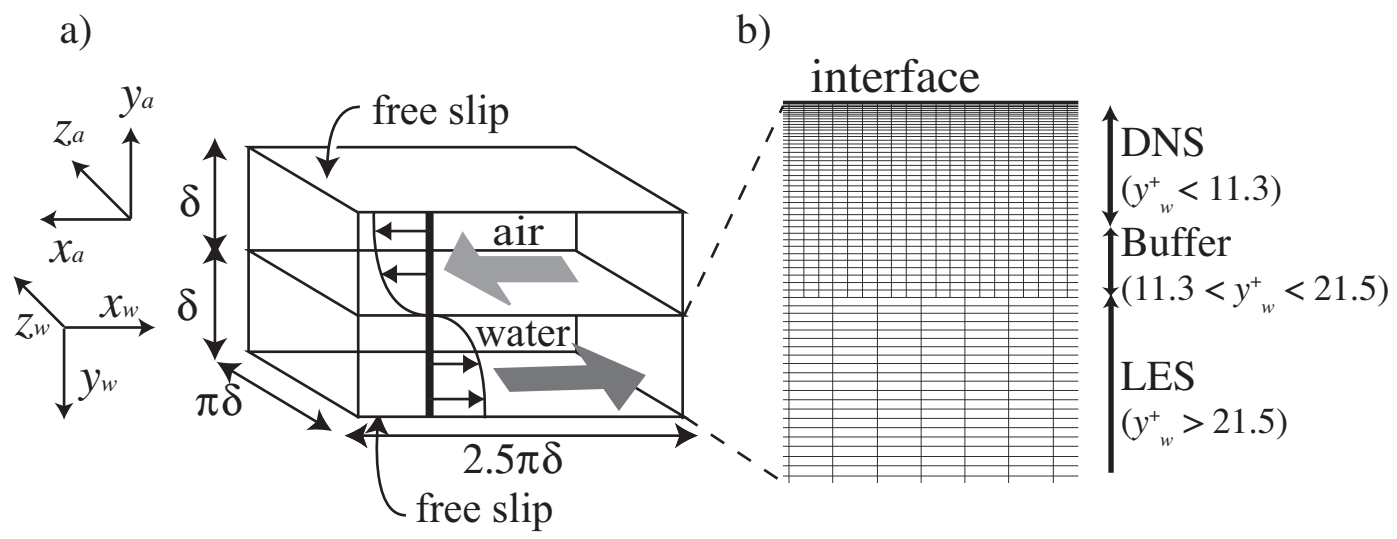


Fig. 1 a) Computational domain and coordinate system, and
 b) grid system in hybrid DNS/LES

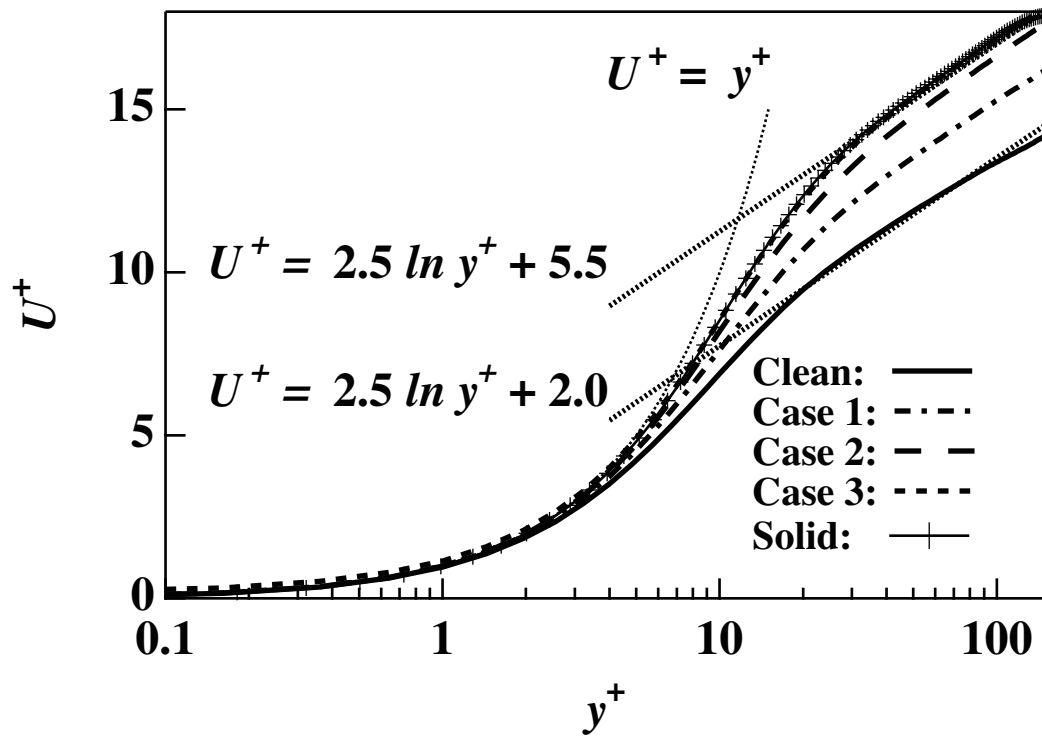


Fig. 2 Mean velocity in the water phase relative to the interfacial velocity.

Figure3

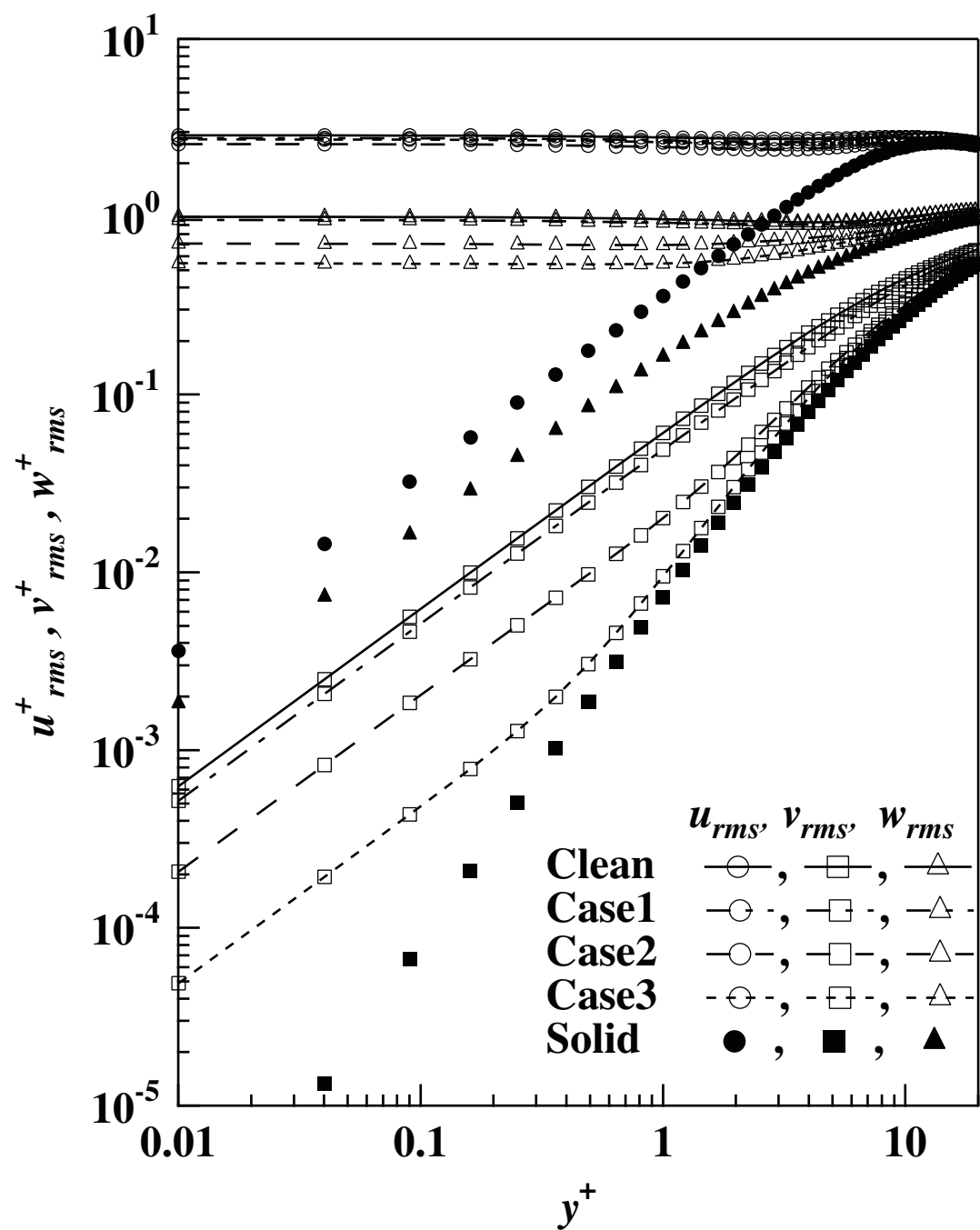


Fig. 3 Limiting behavior of velocity fluctuations close to the interface.

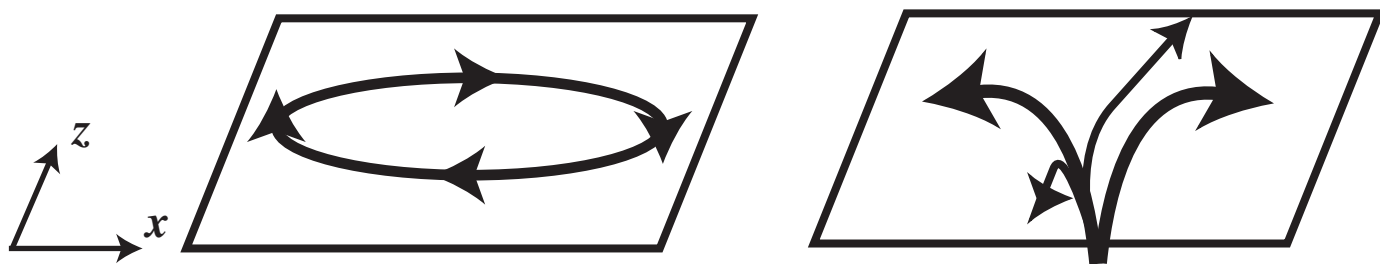


Fig. 4 Decomposition of the interfacial velocity vector into a) solenoidal and b) irrotational components.

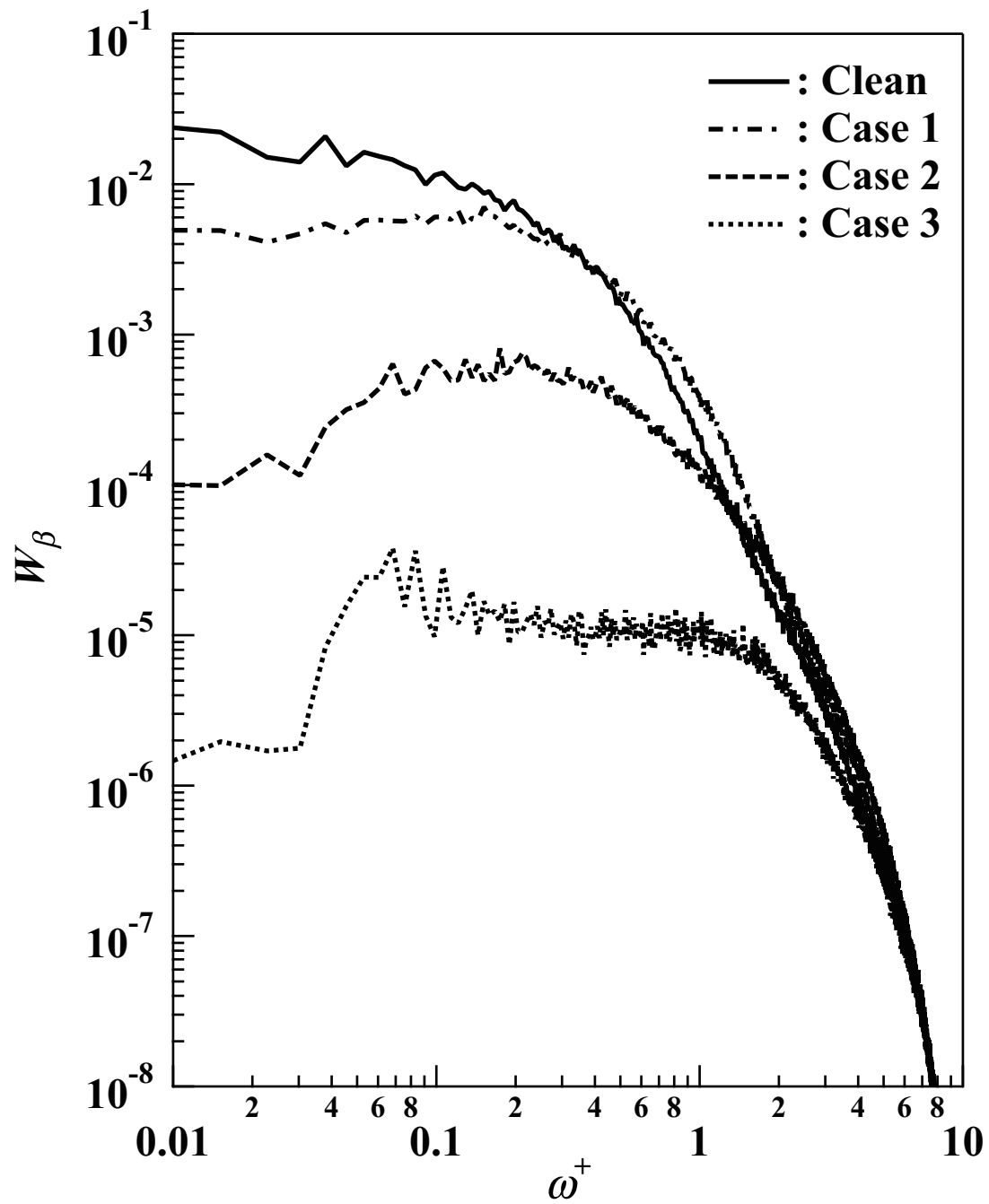


Fig. 5 Frequency spectra of the surface divergence.

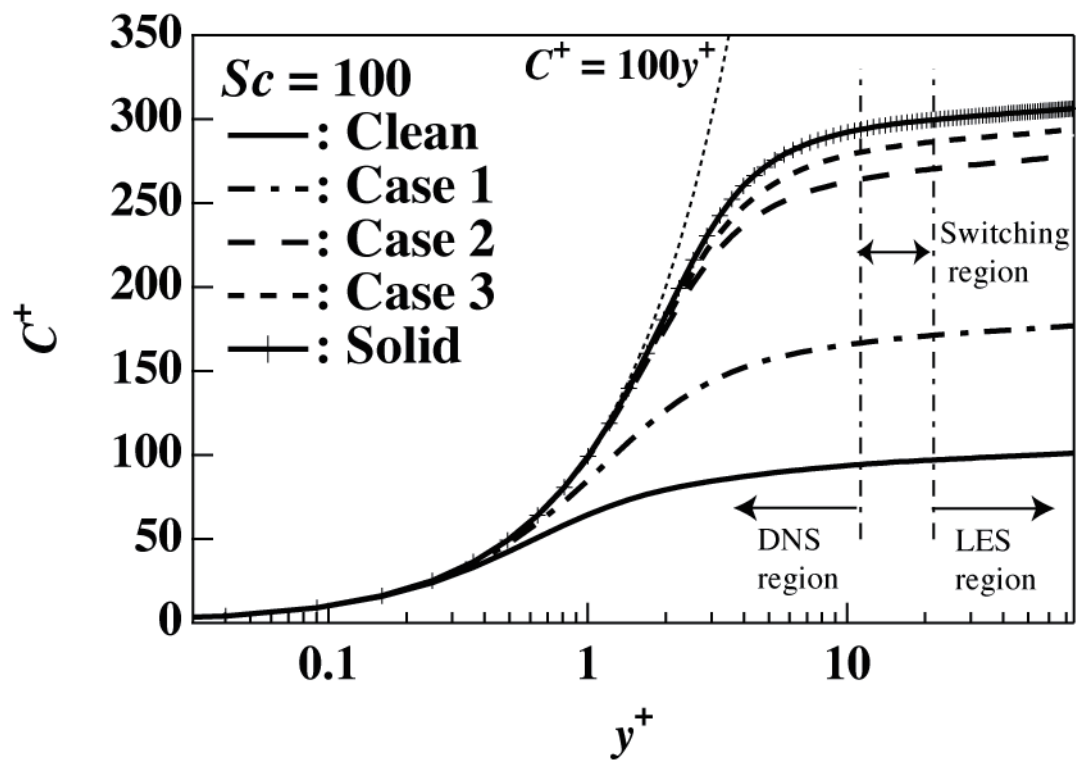


Fig. 6 Mean concentration profiles.

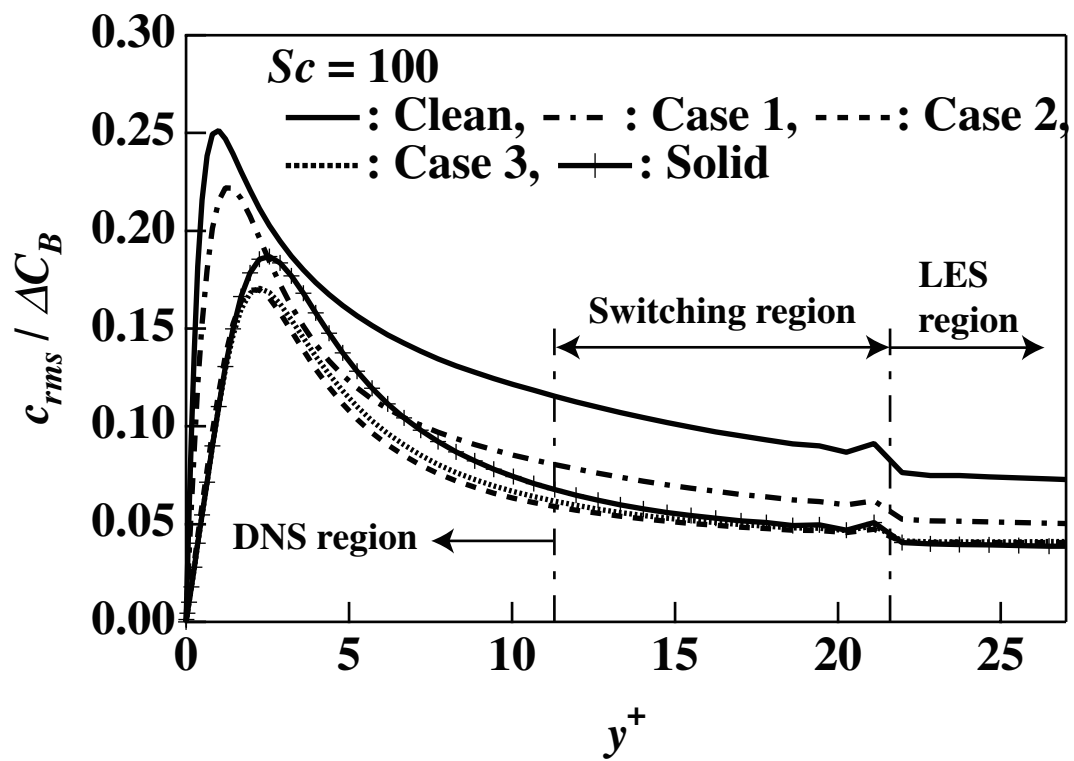


Fig. 7 Concentration fluctuations.

Figure8

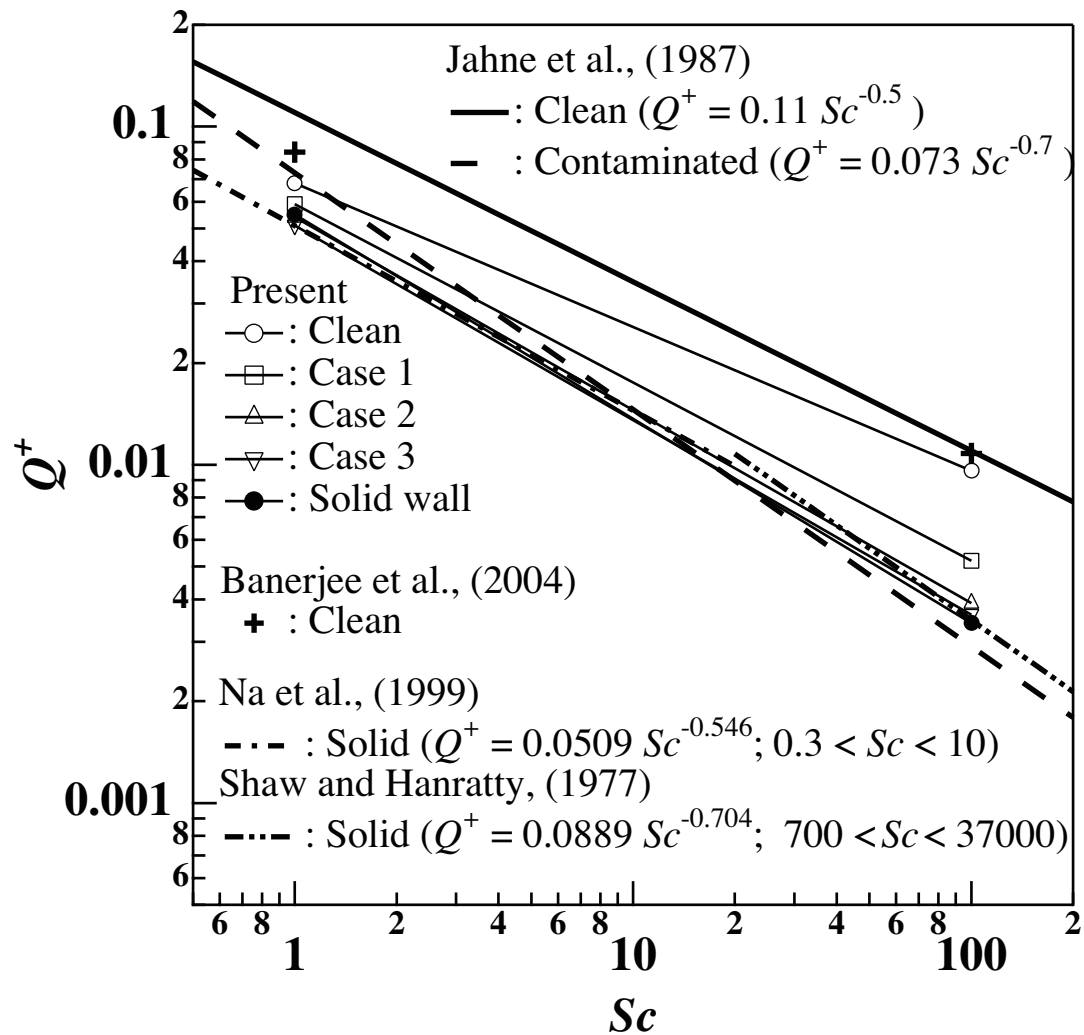


Fig. 8 Mass transfer rates as a function of the Schmidt number.

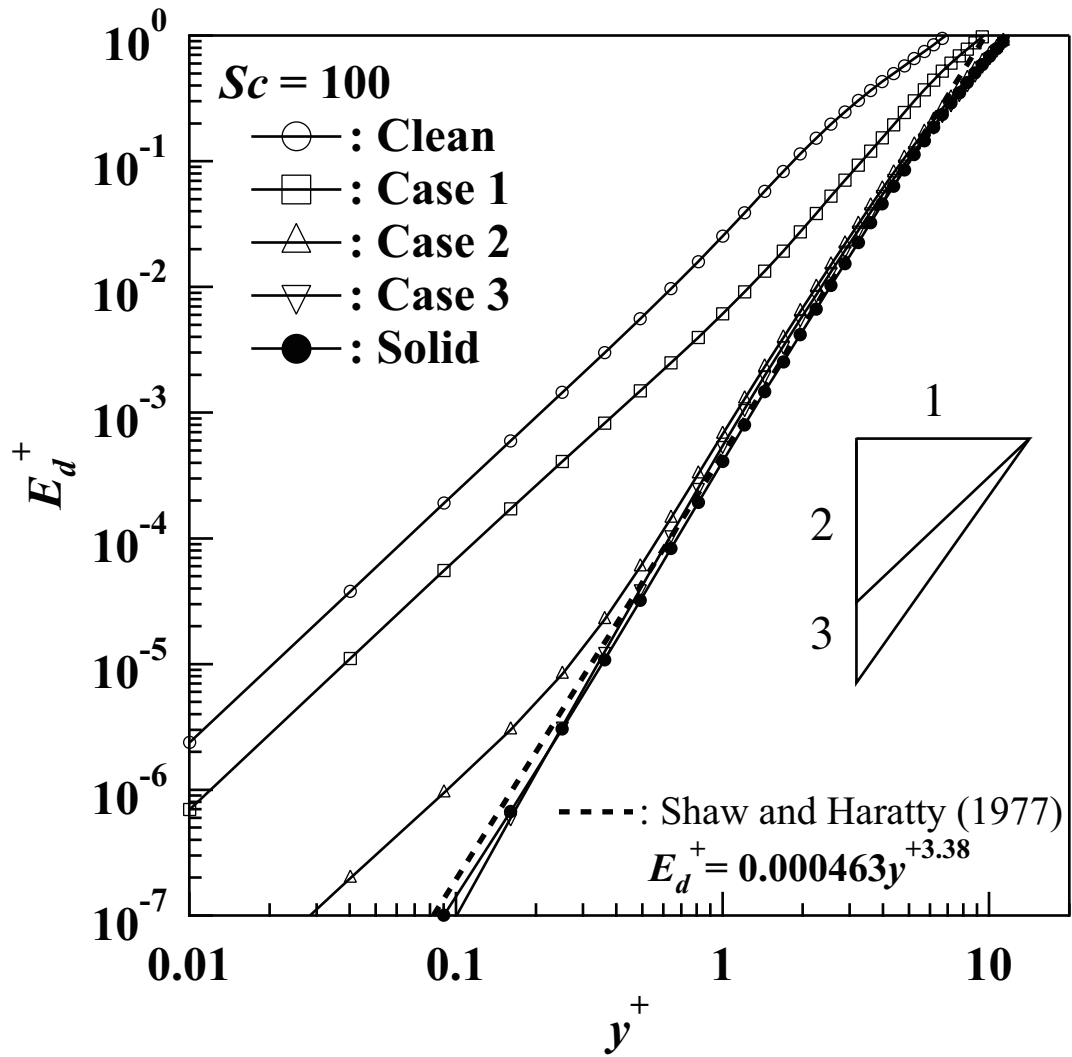


Fig. 9 Limiting behavior of the eddy diffusivity close to the interface at $Sc = 100$.

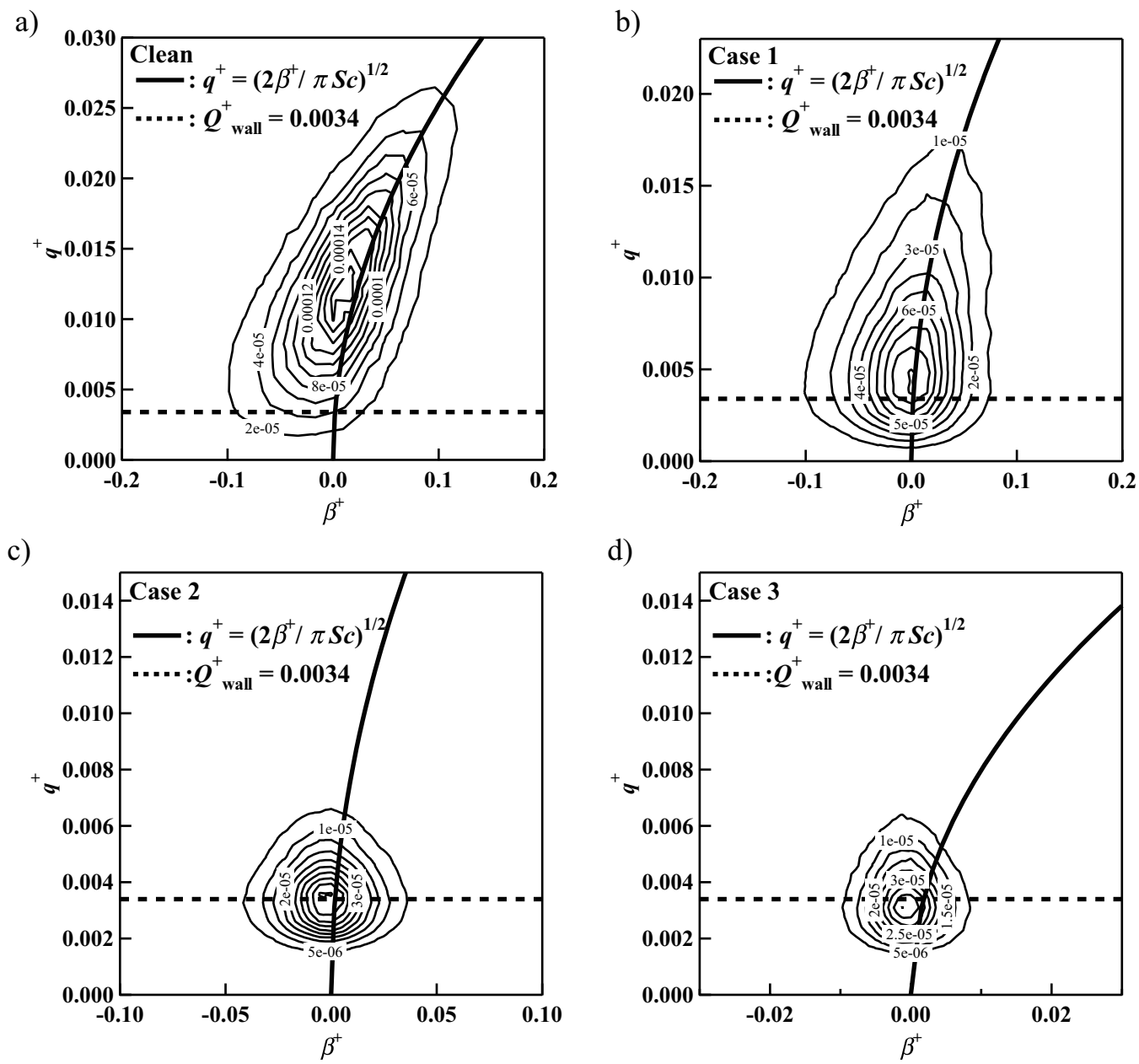


Fig. 10 Contribution of the surface divergence to the interfacial mass flux at $Sc = 100$.

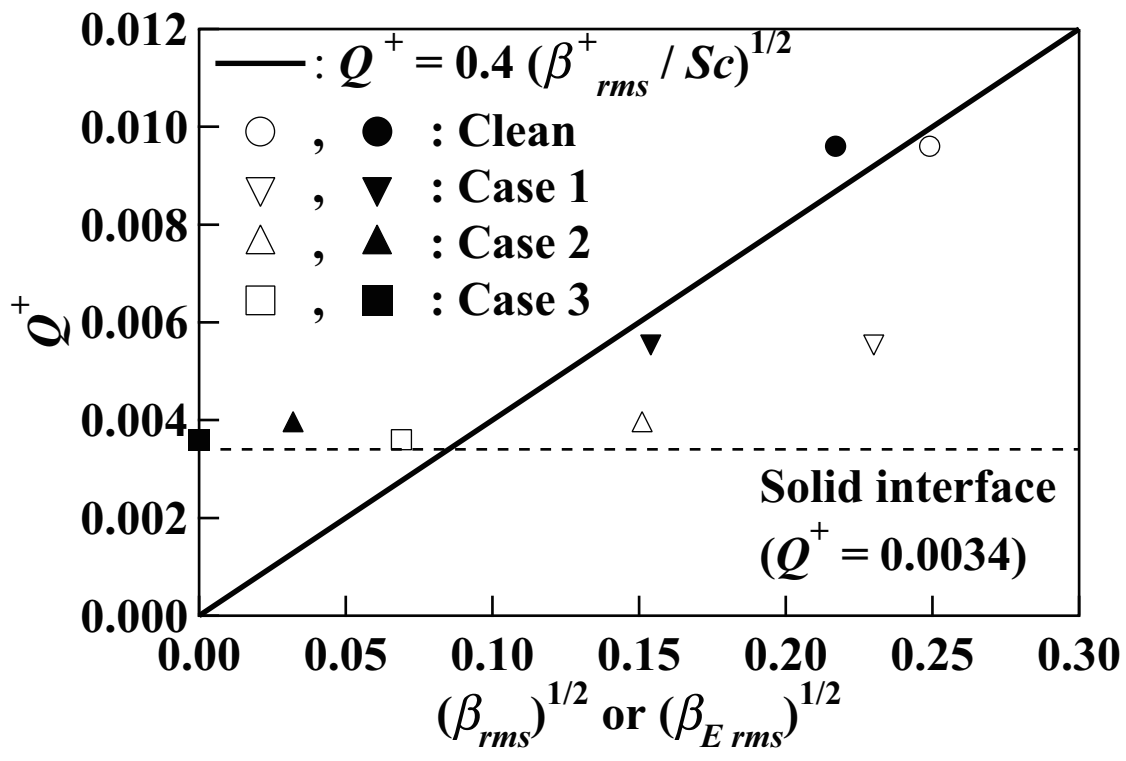


Fig. 11 Mass transfer rates as a function of $\sqrt{\beta_{rms}}$: open symbols and $\sqrt{\beta_{E rms}}$: solid symbols.